We are IntechOpen, the world's leading publisher of Open Access books Built by scientists, for scientists

4,800
Open access books available

122,000
International authors and editors

135M
Downloads

Our authors are among the

154
Countries delivered to

TOP 1%
most cited scientists

12.2%
Contributors from top 500 universities

WEB OF SCIENCE™

Selection of our books indexed in the Book Citation Index in Web of Science™ Core Collection (BKCI)

Interested in publishing with us?
Contact book.department@intechopen.com

Numbers displayed above are based on latest data collected.
For more information visit www.intechopen.com

13

Investigating Optoelectronic Properties of the NbN Superconducting Nanowire Single Photon Detector

Zhizhong Yan
University of Waterloo
Canada

1. Introduction

Superconducting optoelectronic devices have been explored as mixers, and detectors to detect single photons, high energy radiations, e.g. X-rays. This category of devices can be made from either high temperature or low temperature superconductive materials. Recent progresses in the semiconducting counterparts have demonstrated competing and surpassing performance over the most of the superconductive optoelectronic devices. However, nanofabrication technique has been widely used in state of the art superconducting optoelectronic devices, such as single photon detectors and hot electron mixers.

One type of Single Photon Detector (SPD) that are sensitive to a wide spectrum of phone energies, namely Superconducting Nanowire Single Photon Detector (SNSPD) based on niobium nitride (NbN) thin films has drawn intensive interests. Such detectors exhibit remarkable performance, such as high counting rate, low dark count, and low jitter time. The fundamental reason is because of the nano size of the superconducting condensate that is comprised of only a few number of charge conducting carriers, i.e. Cooper pairs. The low operating temperature also helps reduce the thermal noise. These advantages result in a superior environment for converting single photon energies into electrically measurable signals. On the other hand, semiconducting materials, such as InGaAs, although technically it is possible to make geometrically and structurally similar device of semiconductor nanowire meander lines, it is impossible to achieve the same photon-to-electrical (quantum optoelectronic) gain, due to the fact that the charge carriers are Fermionic, i.e. the total wave function of them lacks coherence based on the Pauli-Exclusion Principle; superconducting SPDs, instead are comprised of Cooper pairs, which lead to the Bosonic ensemble acting as a quantum optoelectronic detector. Such unique property not only allows superconducting nanowire device for large dynamic range, but also make it sensitive to much lower energy photons, such as telecom wavelength, or even longer wavelength single photons.

Therefore, investigating photon interaction with Cooper pairs in the superconducting nanowire structure will be the key operation to understand the single photon detection, and to devise novel superconducting optoelectronic sensor, in particular to discover its quantum detecting nature. The photon detection can be viewed as one strong nonlinear effect particularly exhibited in those nanowires. In principle, the strong nonlinearity stems from the strong depletion of Cooper pair density. Either bias current, or incident photon flux, or increased temperature can drive the nanowire into deep Cooper pair depletion regime.

One efficient way to probe the Cooper density is to measure the kinetic inductance of the nanowire structure. The inductance measurement requires an incident RF/microwave power and comparing the reflection power for both amplitude and phase. Since the nanowire makes a very sensitive detector, the incident RF/microwave probing power should be as low as possible. In this chapter, we will present a one-port S-parameter measurement that fulfills the above requirement; and apply the developed method to further investigate the superconductive nonlinearity under combinations of temperature, bias current and optical power.

Microwave measurements have been exploited to examine the nonlinear properties of superconducting materials for many decades. The merit of nonlinearity can be studied by measuring the parametric variation of the Quality factor (Q-factor), surface reactance and resistance of superconducting resonators. Such variation always behaves as a function of frequencies and power levels of the input signal, external magnetic field, or ambient temperature. The nonlinearity can even be found by measuring higher orders of harmonic power spectra.

However, studies on dc current or voltage induced nonlinearity have not yet been performed in the above devices, mainly because they can be treated only distributively, due to their relatively larger geometrical sizes with respect to the operation wavelength. Recently, NbN nanowire meanderlines have extensively been used to make the SNSPD. The total length of the meanderline is typically 500 μm, much shorter than the center wavelength of a photon-induced microwave signal. One can treat the SNSPD as a lumped circuit element, terminating at one end of a normal transmission line, typically a 50 Ω Coplanar Waveguide (CPW) made of Au/Ti. Therefore, new technique is required to explore the DC-bias induced nonlinearities, particularly in the kinetic inductance or natural damped resonance frequencies associated with the meanderline.

Since relatively large but nonlinear kinetic inductance is an intrinsic property of the SNSPD, the relationship between the kinetic inductance and bias current might reveal geometrical constrictions that limit the quantum efficiency (QE). The value of the kinetic inductance also determines the rise and fall times of the photo-induced signal in the SNSPDs. The fall time is associated with the device recovery time, a key timing for the operational speed of SNSPDs. In addition, the nonlinearity of the kinetic inductance can be potentially useful to devise and integrate novel superconducting single photon detectors with parametric amplification transmission lines. Therefore, kinetic inductance and its relationship with electrical bias becomes important figure of merit for SNSPDs.

The NbN nanowire is essentially a one-port passive device, one can readily explore combinations of resistive and reactive components, when it is treated as the load of a transmission line by the S-parameter measurement. However, only the kinetic inductance has been reported in the current bias mode. In this chapter, we will employ such measurements not only to explore the kinetic inductance, and other relevant reactive and resistive components, under either dc current or voltage bias; but also to find the resonant frequency and quality factor of the packaged NbN meanderline. Furthermore, the detail of a one-port S-parameter measurement including the calibration at low temperature is presented in this chapter.

In the following sections, we first construct the model of equivalent circuitry; derive mathematical relations to compute values of the circuit elements; apply our experimental results to obtain the kinetic inductance, the capacitance and the series resistance; and then

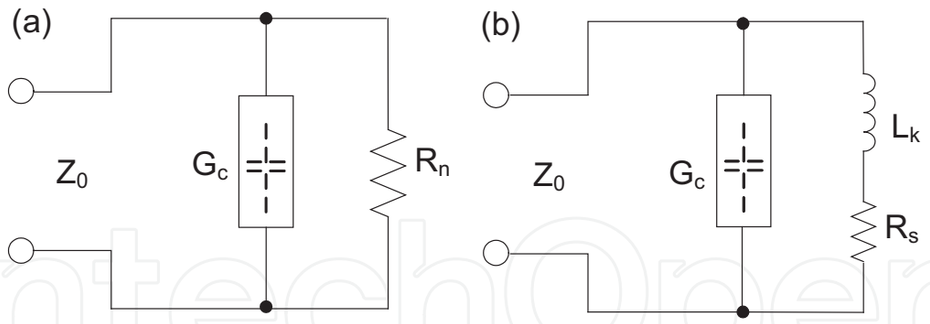

Fig. 1. (a) Room temperature equivalent circuits; (b) Low temperature 4.2K equivalent circuit.

justify the results by the measurement of resonant frequencies and quality factors under various biasing conditions.

More importantly, we would like to highlight that although the methods and experimental procedure in this work are primarily dealing with a NbN superconducting nanowire, these methods and procedures are applicable to other nano size optoelectronic devices, such as high temperature superconducting or even semiconducting optoelectronic devices.

2. Equivalent circuit model for S-parameter measurement

2.1 The construction of the equivalent circuit model

We use the packaged SNSPD identical to what we have reported in (Yan et al., 2009) to undertake all the measurements. However, in the context of current chapter, NbN nanowire meanderlines of the SNSPD are taken as the device under test (DUT). The nanowire meanderline has the same geometrical sizes as what the SNSPD has. For DUT critical temperature T_c, we use an alternative method to find its value. It is estimated to be close to 10.4 K, by the best fitting to the $1-(T/T_c)^4$ like relation based on kinetic inductance-temperature measurement. We will elaborate how to achieve the estimation in later sections. The exact critical current density varies with different DUTs, but all are in the range above $10^6 A/cm^2$.

Since the measurement has to be performed in a packaged device, while the active area of nanowire is relatively small, any distributed effect must be taken into account, including geometrically induced magnetic inductance and capacitance, which are in addition to the kinetic inductance L_k. The former most likely arises from interconnection wires; the latter has been reported either originating from the stray capacitance (Yan et al., 2007; Semenov et al., 2007), or from the dc bias circuitry (Yang et al., 2007). In addition, when the device is dc biased, either with or without the presence of an RF signal, some resistance possibly due to either phase slips or Joule heating may present along the nanowire (Tinkham et al., 2003). We model such lossy contributions by a resistance term of R_s in series with L_k. Therefore, the construction of an equivalent circuit model, which helps to exclude these unavoidable elements, becomes the key to accurately measure L_k, under conditions of both current and voltage bias schemes.

Fig. 1 shows the circuit model at both room and cryogenic temperatures. The procedures to determine values of C, L_k and R_s are deduced from the model, provided that we know the impedance Z_0 of transmission line, and room temperature resistance R_n (usually between 1.5 to 2 MΩ) of the NbN nanowire meanderline. The two-step procedure comprises room and cryogenic temperature S-parameter measurements. Firstly, we perform a room temperature

one port S-parameter measurement to find the value of lumped reactance stemming from geometrical factors. The equivalent circuit is illustrated in Fig. 1 (a). Fig. 2 shows the results of the S-parameter measurement. From the plot, one can find a phase lag whose angle is proportional to the testing frequency. For mathematical simplicity, the phase angle is expressed in wrapped format at $\pm 180^{\circ}$. The phase angle in fact constantly decreases with each increment of measuring frequencies. Such observation confirms that a capacitance does exist. The value of such capacitance can be well evaluated at frequencies of a few hundred MHz, typically at 100 MHz, to avoid errors arising from magnetic inductances.
Note that two assumptions have been made here:

1. The magnetic inductance L_m has not been taken into account. Fig. 2 displays two resonance frequencies at room temperature measurement. Based on the plot, one can estimate the magnetic inductance L_m to be less than 1 nH, which is not subject to the presence of L_k. In comparison with the kinetic inductance L_k of the nanowire of interests, we estimated L_m is less than 1% of L_k. However, it can become significant when very high RF frequency is applied, typically above 5 GHz. In the frequency range below 300 MHz, where our measurements were made, neglecting L_m should not cause any error in the final results of our measurements.
2. One should be aware that the origin of R_s is not entirely clear yet, but it is definitely different from a stable hotspot resistance, especially when the resistance in the voltage bias scheme, after the critical current point. Quasiparticle excitation is most probably responsible for R_s in this range, where electrically spontaneous relaxations can be observed, and L_k exhibits less than three times L_{k0} (the zero bias L_k) change. Beyond this range, where a stable hotspot has formed, we observe an abrupt L_k variation, associated with a similar style of resistance change. We suspect that the long range coherence of the order parameter has been quenched; a hotspot will thus develop by the process of self Joule-heating.

Based on these assumptions, we conclude that the impedance of the capacitance is dominant (illustrated in Fig. 1 as G_c), while the impedance due to the magnetic inductance is negligible in comparison with the impedance of kinetic inductance L_k, at low frequencies typically below 300 MHz. Secondly, when we cool down the packaged NbN meanderline to the cryogenic temperature, the corresponding circuit model is depicted in Fig. 1 (b). Assuming that the capacitance (G_c) keeps constant, the kinetic inductance L_k in series with R_s can be determined by performing a similar one port S-parameter measurement.

2.2 Scattering parameter analysis

Elements of the circuit model shown in Fig. 1 are determined based on S-Parameter (S_{11}) measurement, which can be done by a Vector Network Analyzer (VNA) in a certain frequency range. The inputs of the following mathematical relations are from S_{11} measured at both room and cryogenic temperatures.
The S_{11} can also be expressed as the reflection coefficient Γ. At each given frequency ω, the magnitude $\rho = |\Gamma|$ and phase angle θ can be written as $\Gamma = \rho e^{i\theta}$. We can define the complex conductance G_c as the termination of the transmission line whose characteristic impedance is 50 Ω

$$G_c = \frac{i\,(\Gamma - 1)}{\omega\,(\Gamma + 1)\,Z_0}. \tag{1}$$

where $Z_0 = 50\Omega$, and the complex $G_c = C - \frac{iG_n}{\omega} = C - \frac{i}{\omega R_n}$. The capacitance and the normal state resistance in parallel can be obtained by the knowledge of S_{11} measurement in the room

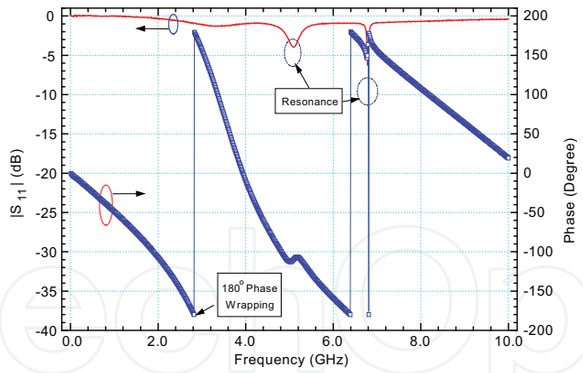

Fig. 2. Room temperature S-parameter measurement, the phase trace (denoted as hollow blue squares) is wrapped at every $\pm 180^{\circ}$ angle.

temperature as

$$C = \frac{-2\rho \sin\theta}{\omega Z_0 \left(1 + 2\rho\cos\theta + \rho^2\right)}, \tag{2a}$$

$$R_n = \frac{Z_0 \left(1 + 2\rho\cos\theta + \rho^2\right)}{1 - \rho^2}. \tag{2b}$$

The room temperature S-parameter measurement indicates that there exists a capacitor that plays a role in the equivalent circuit model. The contribution of this capacitance leads to the resonance behavior. When the meanderline has been cooled down to its superconducting state, the normal state R_n becomes the combination of a kinetic inductance L_k and a series resistance R_s. The series resistance has very small values when the bias current is lower than the critical current I_c. We introduce a complex resistance Z_{Lk} to represent the circuit components when the NbN nanowire is in the superconducting state. It comprises the contribution from the kinetic inductance L_k and the series resistance R_s. The relation between the measured S-parameter S_{11} or Γ and the capacitance C to obtain Z_{Lk} is expressed as

$$Z_{Lk} = \frac{i\left(\Gamma + 1\right) Z_0}{\omega\left[\left(1 + iZ_0\omega C\right)\Gamma - \left(1 - iZ_0\omega C\right)\right]}. \tag{3}$$

After obtaining Z_{Lk}, the kinetic inductance $L_k = \mathrm{Re}\left(Z_{Lk}\right)$ and series resistance $R_s = -\omega \mathrm{Im}\left(Z_{Lk}\right)$ can be measured by separating the real and imaginary parts of the complex Z_{Lk}. With the increased value of R_s, the resonance frequency deviates from the undamped LC resonance frequency ω_o ($\omega_o = \frac{1}{\sqrt{L_k C}}$) as illustrated in the Fig. 1 (b). The deviation of ω_o degrades to the damped resonant frequency ω_d

$$\omega_d = \omega_o \sqrt{1 - Q^{-2}} \tag{4}$$

where the Quality factor Q can be calculated through the relationship $Q = \frac{1}{R_s}\sqrt{\frac{L_k}{C}}$.

3. Experimental results of kinetic inductance measurement

3.1 Experimental setup and measurement principle procedures

The RF/Microwave characterization system of the packaged NbN meanderline employs an Agilent E8364B PNA Network Analyzer (10 MHz to 50 GHz), a Pasternack bias Tee

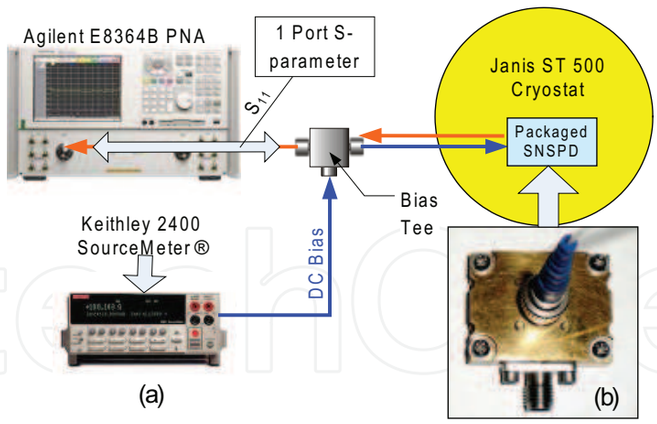

Fig. 3. The experimental setup for the measurement of circuit model elements: (a) The configuration diagram, (b) The photograph of the packaged SNSPD.

10MHz-6GHz, a Keithley 2400 SourceMeter, and a Janis ST-500 cryostat. Their connection is illustrated in Fig. 3 (a). The DUT is packaged in an ETP copper housing equipped with a 40 GHz bandwidth k-connector to maintain the high frequency performance free from the cryogenic temperature stress. The k-connector dielectric layer is made of air/vacuum rather than Teflon in SMA connectors that suffers contraction. In addition, the dielectric constant of Teflon may vary such that it may lead to unwanted variation of the port impedance. The packaged housing is first plated with nickel followed by gold to improve the thermal conduction with the cryostat cold plate. The NbN meanderline is electrically connected by silver epoxy to glue one contact pad to the microwave center pin, and the remaining two pads to the wall of the housing. The final result of the device package is shown in Fig. 3 (b).

The measurement assumes that any extra time delay arising from interconnections within the device packaging is negligible, because of two considerations: (1) The S-parameter S_{11} can be technically measured at only the reference plane, located at input/output port of the packaged NbN meanderline. The reference plane is set by calibration with VNA; (2) The working wavelength (in meters) is much longer than the total electrical wire length (in one hundredths of a meter) including the packaging and the coplanar waveguide on the substrate. Thus, the circuit model in conjunction with its mathematical description has been justified.

It is challenging to do S-parameter measurement under cryogenic temperature and high vacuum because of two limiting factors: (1) We have to limit the amplitude of the ac signal to avoid the device latching when the dc bias is very close to its critical point; (2) The interconnection loss along the transmission line, especially the connector loss, weakens the reflected power. As a result, the ratio of signal to noise becomes extremely low. Since the standard one-port calibration can be performed only in the range of room temperature (approximately 25-30 °C) and pressure (10^3 mbar), the forward tracking error terms in a standard one-port calibration algorithm can not be kept accurate enough, because the portion of the measuring coaxial cable has been cooled far below its calibrating temperature; and has been placed in an ambient of high vacuum condition ($< 10^{-5}$ mbar).

We have observed that the amplitude of Γ in the frequency range experiences about 0.1 dB variation on average. According to our calculation, R_s should be very sensitive to $|\Gamma|$ when the dc bias current is very close to zero, because R_s is expected to be very close to zero. The associated phase angle variation can be approximated in the complex plane by simple geometrical relations and the result indicates the phase angle variation is less than 0.6 degree.

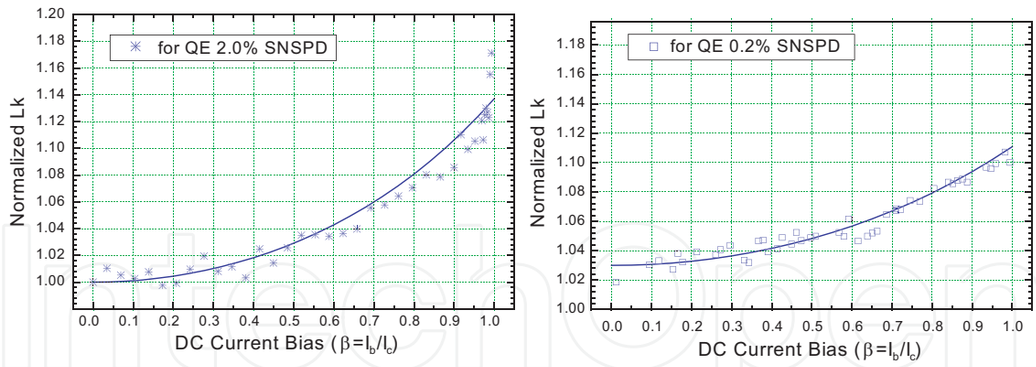

Fig. 4. The measured kinetic inductance for two NbN nanowire meanderlines with different film quality; solid lines are results from theoretical simulations.

Thus, the inductance measurement can achieve a good accuracy, even though the capacitance reduces the phase angle as a function of frequency ω.
In the experiment, we treat the bias tee and cryogenic cable as one lossy transmission line. The calibration is done by setting the reference plane to the end of the cryogenic cable, i.e. the k-connector input of the packaging. Thus, losses from the cryogenic cable, the bias tee and interconnecting components, which are in the ambient temperature, have been compensated by the calibration. The calibration frequency ranges from 10 MHz to 300 MHz. The dc bias source is programmed in either current or voltage mode. The microwave probing power is set at -76 dBm, corresponding to 1 μA peak-to-peak ac current at a 50 Ω coaxial cable. However, considering the cryogenic cable loss, the effective ac current amplitude at the device side falls to about 0.25 μA, which poses much less perturbation to the system during the measurement. Meanwhile, we have observed that when the frequency is higher than about 70 MHz, the S_{11} magnitude variation due to the incident microwave signal becomes negligible. Therefore, the measurement of circuit elements L_k, C and R_s starts with S_{11} frequency points higher than 70 MHz and averages them to the upper frequency limit (in this measurement it is 300 MHz).
Moreover, the choice of calibration power is -30 dBm, whereas the measurement power is set to -76 dBm. This calibration power level is chosen by considering that the minimum noise floor for this VNA preamplifier is -110 dBm. If the calibration power is too low, the forward tracking error term can not be well resolved after the calibration. We can use the data track smooth algorithm as well when we switch the power level down to -76 dBm. However, the smoothing data track can not lead to a higher signal to noise ratio. Instead, we can reduce the *IF bandwidth* to 10 Hz to increase the measurement accuracy. Based on our experiment, further decreasing *IF bandwidth* has no appreciable improvement. In addition, *stepped frequency scanning* is adopted in lieu of the default adaptive scan mode. Each stepped frequency has a 1 ms delay to make sure no residue power affects the adjacent frequencies.

3.2 Kinetic inductance measurement results

Initially, we apply the current bias scheme in the measurements. Fig. 4 shows the measured kinetic inductance for two identical packaged devices, made of NbN nanowire meanderlines. Both measurements of L_k have been normalized to their zero bias kinetic inductance, respectively. The capacitance has been measured in the room temperature via one port S-parameter measurement. The measured capacitance after postprocessing indicates that its value is device dependant. In this work, the capacitance for higher quality film nanowire

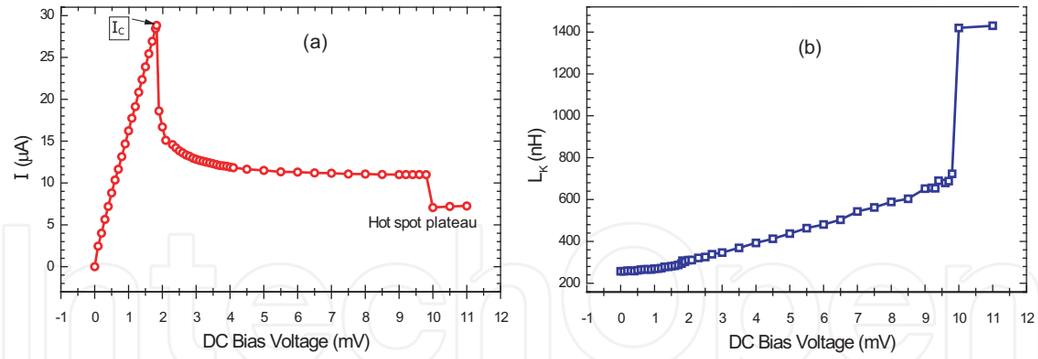

Fig. 5. The linkage of the I-V scan and kinetic inductance variation, (a) the I-V curve under voltage bias scheme; (b) the measured kinetic inductance L_k.

is 1.6 pF; whereas for the lower film quality [1] one, its capacitance is 1.4 pF. On the other hand, the former has zero bias kinetic inductance at about 210 nH; while the latter is 230 nH. In both cases, the nonlinear kinetic inductance displays a trend of higher L_k associated with a higher bias ratio. Detailed discussions on the theoretical background are presented in Appendix A. The relationship of L_k with respect to the bias current ratio is given by (5); and the simulation results are plotted as solid curves in Fig. 4.

However, neither in this work nor in the relevant literatures (Miki et al., 2008; Hadfiled et al., 2007) have shown any abrupt change of L_k when the dc bias current is very close to the so-called critical current I_c, even when we are able to drive the bias current ratio above 99%. Since the kinetic inductance L_k by definition should be inversely proportional to the Cooper pair density of the nanowire condensate, this seems to imply that the I_c may only be a local effect, possibly a resistive spot somewhere along the nanowire. Further increasing the bias current above I_c will cause device permanent latching .

Based on the preceding analysis, we switch our dc bias scheme into voltage bias. Now all of the measurement conditions are kept the same except the bias method. Fig. 5 demonstrates the linkage between the different I-V regimes and the kinetic inductance L_k of the NbN meanderline. The curve shows that even when the bias current decreases after I_c, the kinetic inductance increases constantly with the increasing bias voltage. This suggests that Cooper pairs are proportionally accelerated by applied voltages without apparent resistance barriers along the meanderline path, until the hotspot formation plateau occurs. At that transition point, the kinetic inductance changes very abruptly to 1500 nH at 4.2 K. In order to see the connection of the increasing kinetic inductance L_k with the series resistance R_s, Fig. 6 shows the measured L_k and R_s at each bias voltage point. The figure suggests that when the bias voltage surpasses the point where I_c occurs, both L_k and R_s follow the same trend of a constant increment, due to dissipations caused by the quasiparticle excitation. At lower dc bias, such dissipation is weak, so R_s is negligible. R_s increases smoothly from zero to a quasi stable value close to 120 Ω prior to the formation of an initial hotspot, whose stable value is about 500 Ω. This process can *not* be found in the dc current bias scheme. Instead, when it is switched to the voltage bias, we observe a continuous transition for kinetic inductance L_k and series resistance R_s. They both display an abrupt change at the point where the dc bias current drops below the return current I_{ret}, as shown in Fig. 5(a). The abruptly changed value of R_s is in the range of the hotspot resistance R_h. Very large variations of L_k (more than four times $L_k(\beta = 0)$ have

[1] The higher SNSPD QE, the better film quality. So the better thin film quality one is equivalent to higher QE SNSPD.

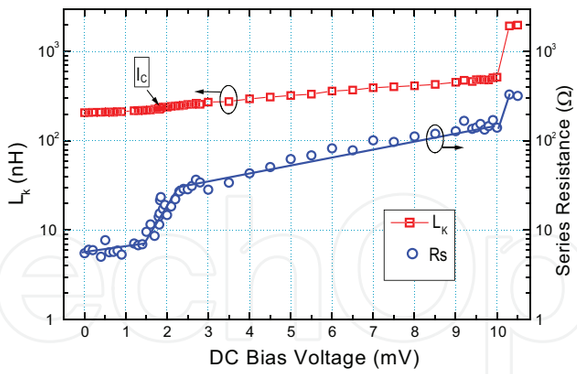

Fig. 6. The measured kinetic inductance and series resistance under the voltage bias scheme for the SNSPD whose QE is 2%.

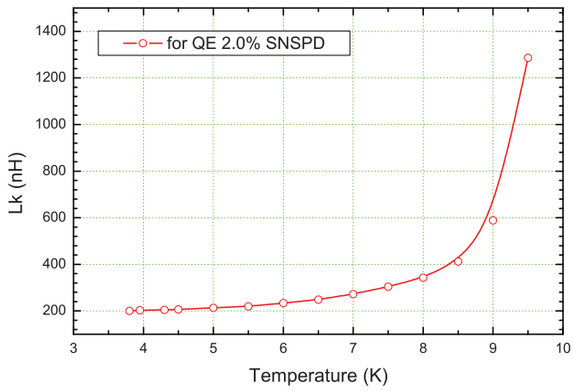

Fig. 7. The measured kinetic inductance by varying the thermal bath temperature in the absence of optical irradiations.

been observed, and show good agreement with the Ginsburg-Landau (G-L) theory prediction (Yan et al., 2007), when R_s becomes comparable with the R_h. Such experimental observation suggests that when the NbN nanowire meanderline is used as SNSPD, its photon-response due to the formation of hotspot strongly correlates to the abrupt change of kinetic inductance. We performed the L_k measurement by changing the DUT temperature. The temperature is monitored and controlled by the Lakeshore 332 two channel temperature monitor/controller. This temperature controller is equipped with two independent channels of heater and thermal sensor interface. The helium flow of the cryostat is also adjusted in order to track the change of temperature and to keep the temperature of the ST-500 cold plate as stable as possible. The temperature has the fluctuation less than 0.1 K. We average our measurements over one particular temperature for multiple times to reduce the uncertainty.

The same one-port S-parameter measurement as what we have performed in the first section is undertaken. L_k is measured as a function of temperature T. The result is depicted in Fig. 7. The open circle in the plot is the experimental measurement; the solid line is the fitting curve using a asymptotic relation of $1-(T/T_c)_0^{\alpha}$. We take $\alpha_0 = 4$, and $T_c = 10.4K$ for the best fit to the measurements.

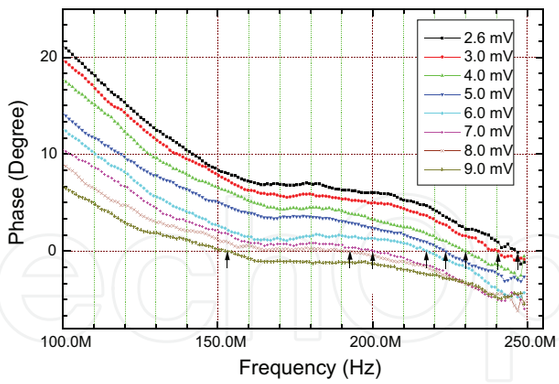

Fig. 8. The measured kinetic inductance and series resistance under the voltage bias scheme for the SNSPD whose QE is 2%, the arrows indicate frequency points of each damped resonance.

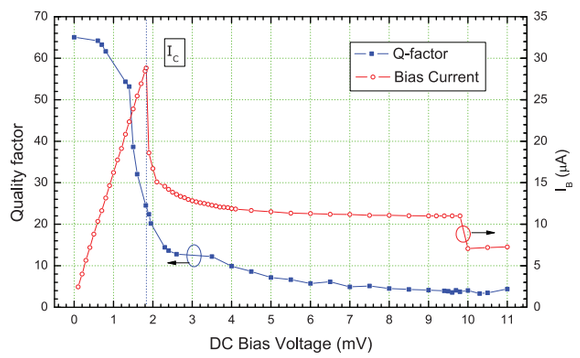

Fig. 9. The quality factor -Q of the equivalent R_s-L_k-C circuit as the resonating circuitry

3.3 The resonating circuit analysis

To further confirm the validity of the R_s-L_k-C circuit model and the related model parameter measurement, one can resort to resonance frequency measurement, i.e. by looking at the frequency points where the phase angle of S_{11} is zero. In this case, the load at the end of the transmission line has no imaginary component. The undamped resonance happens when R_s is zero or negligibly small. What is important for this work is that the damped resonance frequency ω_d deviates from the undamped resonance frequency (ω_o) governed by Eq. (4), due to large values of R_s. Fig. 8 shows the experimental results of the phase with different frequencies of the RF/microwave excitation signals under different bias voltages. The values of L_k and R_s for each branch can be found in Fig. 6.

Fig. 9 displays the extracted quality factor as a function of bias voltage. The plot indicates that the quality factor for this photon detector is not high. Unlike the high-Q resonator detection mechanism, the highest Q of the SNSPD is less than 100 at 4.2K. We think that it is beneficial for the fast resistive state formation. The Q-value is expected to increase with lower temperatures than 4.2 K, but it makes the transition from superconducting to resistive state hard. Therefore, experimentally the QE of SNSPD has not been reported to be further improved when its operating temperature is below 1.8 K.

Table 1 tabulates the calculated undamped resonance frequency (ω_o) and the directly measured damped resonance frequency (ω_d). The corresponding Quality factor Q is obtained

Voltage (mV)	L_k (nH)	Undamped $f_0 = \frac{1}{2\pi\sqrt{L_k C}}$ (MHz)	Damped Exp. resonance f_d (MHz)	Q-factor[a] Q	Q-factor[c] Q
9.0	456.00	186.33	153.40	1.75	4.15
8.0	415.16	195.28	192.25	5.56	4.52
7.0	395.50	200.07	200.65	12.50 [b]	4.90
6.0	362.13	209.09	217.45	3.45 [b]	5.75
5.0	323.69	221.15	223.75	6.67 [b]	7.18
4.0	297.35	230.74	230.5	12.5	9.93
3.0	272.66	240.96	240.55	16.67	14.46
2.6	257.50	247.95	246.85	11.11	12.80

a. The quality factor Q is calculated by $Q = \left(\sqrt{1-\left(\frac{f_d}{f_0}\right)^2}\right)^{-1}$.

b. Absolute value $\left|1-\left(\frac{f_d}{f_0}\right)^2\right|$

c. The quality factor Q is directly obtained by the definition $Q = \frac{1}{R_s}\sqrt{\frac{L_k}{C}}$

Table 1. Measured resonance frequencies and kinetic inductance.

by both methods of damped resonance frequency, and the Q factor is defined as the function of L_k, R_s and C. The comparison of both approaches shows a good agreement when R_s is relatively large, e.g.$> 100\Omega$.
The resonating R_s-L_k-C circuit does not display any absorption dips at the resonating frequencies, if we focus just on the amplitude of S_{11}, because of two factors: First, the equivalent circuit shown in Fig. 1(b) is neither a parallel nor a serial typical RLC resonating circuit as depicted in (Pozar, 1998). One can convert our equivalent circuitry into a typical parallel R_s-L_k-C resonator circuit by invoking circuit theories, but the converted parallel resistance becomes considerably larger than the 50Ω transmission line impedance, resulting in a pure parallel L_k-C circuitry approximately. Second, at the non-resonating frequencies, the total impedance of our equivalent circuit becomes primarily reactive, so the unitary reflection will be most probably measured.

4. Ginsburg-Landau relation for kinetic inductance and bias current

In the past, many experimental measurements showed that (a). in dc I-V measurement, even at 4.2 K, there is a non-trivial dc current dissipation, i.e resistance, (b) the residual resistance close to 20 K has the highest value compared with that at room temperature, with resistivity of 200 $\mu\Omega$-cm. To seek more insights, we explored extensively in the relevant literatures; and two well-established evidences have been brought to our attention:

1 The fabrication process of NbN thin films involves sputtering pure niobium target in a mixed gas flow of nitrogen and argon (Keskar et al., 1974). The film properties have been studied microscopically in (Shy et al., 1973)-(Tyan & Lue, 1994), in order to systematically show the weaklink properties of NbN thin films. The electrical properties of NbN thin films have been studied in (Kampwirth & Gray, 1981)-(Gray et al., 1985). Based on values of the normal state resistivity, which is in the range of some 200 $\mu\Omega$-cm, granular boundaries inherently existing in NbN thin films were attributed to tunneling weaklinks. Very interestingly, ref. (Kampwirth & Gray, 1981) gives a good approximation

to the critical current density based on quasiparticle tunneling by Ambegaokar *et al.* (Ambegaokar & Baratoff, 1963)-(Ambegaokar & Baratoff, 1963). We have found out that the normal state resistivity of the nanowire is about 200 $\mu\Omega$-cm, which is the range of granular tunneling range at 20 K regime as discussed in (Kampwirth & Gray, 1981)-(Gray et al., 1985).

2 Microwave nonlinear surface resistance Z_s: NbN has been long employed in microwave applications, primarily useful for making transmission lines and resonators. The power handling capability of such devices has been a topic for many decades (Chin et al., 1992)-(Boin & Safa, 1991). The nonlinear dependency of the surface resistance has been attributed to the granular nature of NbN thin films (**?**), (Chin et al., 1992)-(Boin & Safa, 1991), that has been prepared by the RF sputtering technique. The dependency has been modeled on the basis of tangential magnetic field that is parallel with the superconducting surface. The model involves magnetic field penetration depth. This does not seem applicable to our case directly, because the DUT acts only as a lumped load; but the dissipation of microwave power by granular boundary remains the same mechanism to account for the nonlinearity.

Additionally, we also calculated the phase-slip induced I-V relationship at the transition from the superconducting state to the normal state when the temperature increases across the transition temperature T_c. The exponential increase of resistance indicates the pronounced existence of phase-slip centers in the nanowire meander-line. We suspect that these phase slip centers stem from the granular boundaries during the formation of thin film. It is well known about the process of sputtering thin films. Some seeds of metallic grains expand and gradually merge into one continuous film. Thus, we conclude that the superconducting nanowire is patterned on such thin film and its weaklink effect has to be considered in almost every testing, such as dc I-V and RF/microwave measurements.

Thus, we heuristically conclude that the strong-weaklink network (**?**), or inhomogeneities of the order parameter in one dimension superconducting nanowire, is responsible for both nonlinear kinetic inductance and resistance. The amplitude of complex order parameter has been reduced on average, allowing the G-L equation to be valid in a wider temperature range, e.g. at $0.5T_c$.

We have developed a relation of current bias ratio with respect to kinetic inductance L_k for a clean, uniform bulk superconducting 1-D wire, with the absence of magnetic field, in (Yan et al., 2007), and the analytical solution reads

$$L_k(\beta) = \frac{L_{k0}}{1 - 4\cos^2\left(\frac{\pi}{3} - \frac{1}{3}\arctan\left(\frac{\sqrt{1-\beta^2}}{\beta}\right)\right)} \tag{5}$$

where L_{k0} is the zero bias kinetic inductance. It is device dependent, and can be measured via the method in this paper when the setting dc bias to zero. $\beta = {I_b}/{I_c^{GL}}$ is the ratio of dc bias current I_b to that of bulk critical current I_c^{GL}. Since the order parameter has been reduced due to the strong weaklink network, the (5) is valid for temperature at 4.2 K. However, attention has to be paid to the fact that $I_c^{GL} \gg I_c$, where I_c is defined as the critical current in the context of SNSPD. In terms of thin film quality, or QE of a given SNSPD in the literature, we substitute β with $\beta_b = \gamma\beta$, in which γ is a figure of merit of the thin film quality, defined as $\gamma = \frac{I_c}{I_c^{GL}}$, and $\beta_b = \frac{I_b}{I_c}$.

Parameter	SNSPD # 1[1]	SNSPD # 2[2]
J_c (A/m^2)	6.2×10^{10}	3.7×10^{10}
L_k (nH) [3]	200	230
ρ $(\mu\Omega \cdot cm)$	195	214
λ_L (0) (nm)	383	411
λ_{GL} (0) (nm)	400.7	407.9
λ (0) (nm)	490.6	499
ξ_0 (nm)	6.18	5.91
l_{tr} (nm)	3.97	4.00
κ_{GL}	70.88	73.45

[1]Device QE is 2%
[2]Device QE is 0.2%
[3]Extracted at $T = 4.2$ K with $T_c = 10.4$ K for all calculations

Table 2. Computed superconducting material parameters

Note that technically I_c^{GL} can not be measured directly, but can be deduced through the ratio of $\frac{L_k(\beta_b)}{L_{k0}}$ when $\beta_b \simeq 1$ based on the relationship of (5). Evidently, the highest γ can be close to 0.6 at temperatures of 4.2 K . It would become relatively higher when the temperature is decreased, but we anticipate that γ will saturate at some point due to the possibility that the weaklink will limit I_c from going close to I_c^{GL}. For two of our DUTs, the higher quality one has $\gamma = 0.5$; and $\gamma = 0.4$ for the lower one.
Finally, the effort to account for nonlinear resistance is more complicated, because it involves combinations of material, processing, electrical and thermal physics. The difficulty is added because of the quasiparticles are involved in the presence of RF field. The strong fluctuations of R_s result not only from the quasiparticle generation and recombination process, but also from their tunneling through the weaklinks. We think that detailed discussions are much beyond the scope of this thesis, and we will address this topic in the future works.

5. NbN superconducting thin film properties

We treat superconducting nanowire devices as a nonlinear load of a 50 Ω transmission line. The incident RF/microwave power (ac current) is weakly applied. The reflected power is measured and analyzed as discussed in the preceding sections. Series of experimental results to measure kinetic inductance L_k to study the nonlinearities stemming from dc bias by one port S-parameter measurement. The weak ac current was used (less than 1 μA) as a probe for all measurements.
By knowing the kinetic inductance of the superconducting nanowire via the method described in the preceding section, we are able to obtain some insights to the material properties of the superconducting parameters that is prepared for making NbN SNSPD. After post processing the measured S-parameter, we are able to retrieve London penetration depth, coherence length, and very importantly the first and second critical magnetic field H_{c1} and

H_{c2}. However, the second critical magnetic field intensity can not be simply computed for NbN thin film, especially for the ultra thin film (e.g. 4 nm).
The extraction of values of the penetration depth λ is based on the relations in Ref. (Orlando et al., 1979). The normal state electron specific heat $\gamma_0 = 2.1 \times 10^{-4}\ J \cdot cm^{-3} \cdot K^{-2}$ is from (Johnson et al., 1996). All of the input parameters, including the kinetic inductance L_k in conjunction with the critical current density J_c and the normal state resistivity ρ_n at 20 K are measured parameters. We have also evaluated BCS coherent length ξ_0 and electronic mean free path l_{tr}. Interestingly, we have found that they are comparable. Consequently, all values of different penetration depth are becoming comparable accordingly, which is significantly different from the bulk properties of NbN. This exceptionally long mean free path seems to arise from the two magnitude lower electron gas density at Fermi surface than that of bulk superconductors. Table 2 lists all of input parameters and output results for this evaluation. Oates *et al.* (Oates et al., 1991) reported the penetration depth $\lambda(0)$ obtained from their surface impedance measurement in the microwave range. The comparison shows that our penetration depth value is in good agreement with their results provided that thin film modifies the values of BCS coherent length ξ_0 and mean free path l_{tr}. As a result, their London penetration depth $\lambda_L(0)$ becomes considerably lower than $\lambda(0)$ due to the high ratio of ξ_0 to l_{tr}.

6. DC I-V measurement in the absence of optical power

The dc I-V measurement of the NbN nanowire shows four distinct regimes. The first regime is the superconducting regime and the slope of I-V curve is primarily determined by the cryogenic cable resistance; The second is the switching state (Lindgren et al., 1996), in which spontaneous thermo-electrical relaxation oscillations is dominantly observed; The third regime is the formation and expansion of a stable hotspot, which is the starting point of a self-heating effect. The hotspot grows up with the increment of dc bias to occupy one entire segment of the nanowire. After this point, the fourth regime is entered when one segment of the nanowire becomes a hotwire and starts to heat up the adjacent segments of nanowires.

6.1 Superconducting and switched states

For the first two regimes as demonstrated in Fig. 10, the figure depicts the forward I-V curve obtained via two scan speeds: fast computerized scan and slow manual scan, in which the inset panel displays a typical computerized scan in both forward and backward directions. The manual mode is persistently useful for the small signal S-parameter measurements. In both manual and computerized scan modes, the return current, which manifests the plateau of a hotspot formation, shows the same value. However, the occurrence of this point in the manual scan mode is different from the computerized fast scan mode. For the former mode, it occurs at higher voltage than does the latter, but the latching current (approximately 7 μA) is almost identical. We attribute this to three possible mechanisms: scanning speed, scanning direction and electrical grounding. The manual mode always has slower variation of bias voltage. The voltage relaxation induced by quasiparticle excitations results in a metastable states, which is very susceptible to external perturbations, such as a sudden bias voltage variation, and then stabilizes itself at the latching current.
In addition, the scanning direction depends on whether it starts from a higher bias voltage down to zero (backward), or vice versa (forward). Within the switched states as defined in (Lindgren et al., 1996), the nanowire will exhibit a hysteresis I-V curve due to the thermal healing of the hotspot, i.e. the voltage scans of the forward and backward mode show the hysteresis behavior; and the measured current remains at the level of latching current until

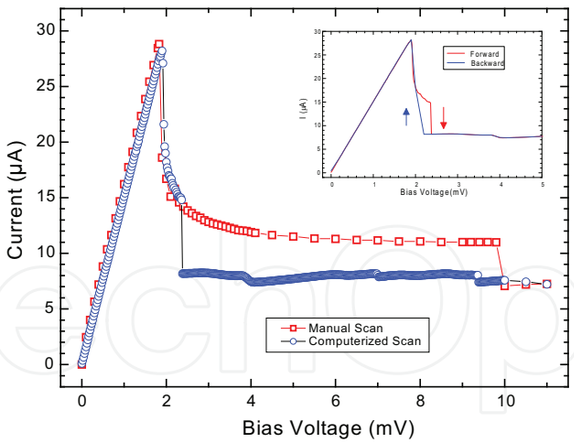

Fig. 10. Experimental voltage and current relationship measured via both manual and computerized scan modes under forward voltage bias scheme; inset panel is a computerized scan curve in both directions.

the bias voltage decreases below the forward latching voltage point. The detail theory has been discussed by Tinkham *et al.* (Tinkham et al., 2003). However, the theory can not account for the different hysteresis loops in two scan modes. We suspect that the electrically shared ground of the analog and digital parts in the source meter is responsible for the difference. In the computerized scan mode, communication between the source meter and computer can induce extra ground voltage fluctuations. Consequently, a smaller hysteresis I-V curve results as demonstrated in the inset panel of Fig. 10.

The dc I-V curve measurement also indicates that when I_b is greater than $\sqrt{2}I_{ret}$, it is no longer a single value function of bias voltage. On the other hand, for any given bias voltage, there exists a single-value current. Lindgren *et al.* used to bias an HTS bridge in the switched state to measure photoresponses (Lindgren et al., 1996). The values of R_s by small signal RF/microwave measurement results in less than 20 Ω, even when I_b is 0.5 μA less than I_c (28.5 μA in this case), which is much lower than the stable resistance of a hotspot by Joule heating.

6.2 Temperature dependent I_c

The critical current I_c can be experimentally determined for a given SNSPD by inspecting the maximum current in Fig. 10. [2] The temperature dependence of I_c can be experimentally found by inspecting the maximum current in the dc I-V measurement at all temperatures. Fig. 11 illustrates the measured zero maximum current for the DUT with higher QE. In the figure, the dot line is a linear fitting curve, whose slope is -5.88 $\mu A/K$; the zero temperature I_c is projected to be 50.74 μA. The red square in the plot is the DUT provider measured I_c at 2 K, which is below the linear fitting trend line. When the temperature ranges from 7.5 K to 9.5 K, approximately a second slope can be observed. Higher 9.5 K, we can only measure submicron ampere current, which is hard to identify it as a maximum current. The linear relation of I_c with the decreased temperature is not consistent with what Ginsburg-Landau theory predicts in the bulk superconductors, from which we expect a relation like $I_c \propto T^{-3/2}$ curve. We

[2] when the bias current I_b is close to I_c, the superconducting nanowire will exhibit a considerable dc resistance primarily due to voltage spikes arising from dark count. Consequently, this will affect the accuracy of the I_c measurement, as well as latching problem in the experiment.

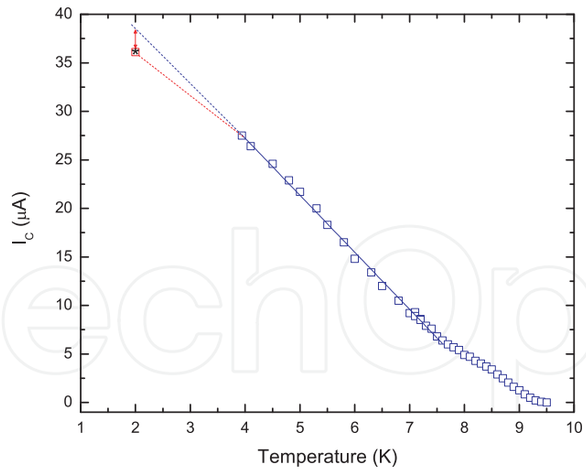

Fig. 11. The zero voltage maximum current, or critical current I_c vs temperature dependence for the SNSPD of higher QE.

attribute the linear relationship of $I_c(T)$ particulary exhibited in the SNSPDs to the NbN thin film, in which the superconducting weaklinks formed during its fabrication process.
The NbN thin film is sputtered on sapphire substrates; and is studied in (Kampwirth & Gray, 1981)-(Gray et al., 1985). The weaklink inherently presents during the ultra thin film sputtering, due to the formation of granular grain boundaries. Kampwirth *et al.* (Kampwirth & Gray, 1981) approximated the critical current based on the quasiparticle tunneling, which is studied by Ambegaokar (Ambegaokar & Baratoff, 1963)-(Ambegaokar & Baratoff, 1963). We can relate I_c to the granular size of the NbN thin film a_0

$$a_0 = \frac{\pi A \Delta(T)}{2 I_c q_e \rho_{20K}} \tanh\left[\frac{\Delta(T)}{2 k_B T}\right] \tag{6}$$

where k_B is the Boltzmann constant; q_e is the electron charge; $\Delta(T)$ is the temperature dependent BCS energy gap; A is the cross section area of the nanowire, and ρ_{20K} is the resistivity and will be addressed later in this section. The value of a_0 provides a quantitatively commencement point in the self-heating model for the SNSPD nanowire that will discussed next.

6.3 Modeling of superconducting and switched state

The I-V curve shown in Fig. 5 (a) prior and after the critical current I_c point, is the superconducting and switched state (Lindgren et al., 1996), respectively. For the latter, it is characterized by a spontaneous relaxation oscillation at about 800 KHz counting rate, when we use the method to perform photon/dark count characterization in (Yan et al., 2009).
Hadfield *et al.* (Hadfield et al., 2005) suspected about 5000 Josephson Junction-like behavior exhibited in their SNSPD, which has the identical geometrical size as that of our DUT. It is actually in consistency with what we calculated based on what Kampwirth (Kampwirth & Gray, 1981) estimated about the single granular size of 100 nm. We further developed a lump 5000-stacked Josephson Junction circuit model to simulate to the total current driven by a voltage source. The voltage source spans from 0 to 10 mV. The simulation results is plotted in a solid curve in Fig. 12. The comparison to the experimental result in the figure indicates that the simulation does not display a relatively flat current in the switched state. This is

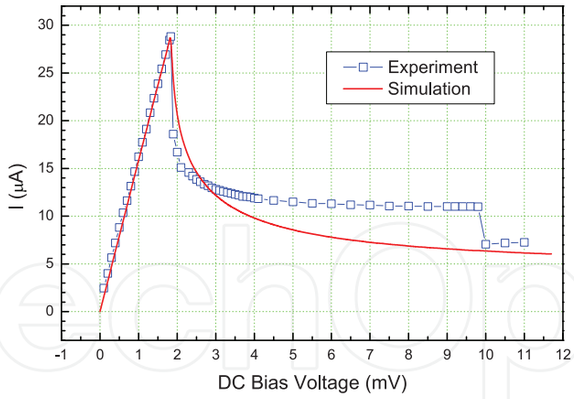

Fig. 12. The simulated dc I-V scan by voltage bias in superconducting and switched states

Name Description	Return Current I_r (μA)	Ambient Temperature $T_b(K)$	Heat Transfer Coefficient $\alpha(W/m^2 \cdot K)$	Resistivity at 20K $\rho_{20K}(\Omega \cdot m)$
DUT ♯1	5.66	4.2	2×10^4	2.05×10^{-6}
DUT ♯2	3.96	4.5	2×10^4	2.14×10^{-6}

Table 3. The self-heating hot spot model parameters

primarily due to the fact that the spontaneous voltage oscillation at about 800 KHz has not been considered in the simulation. The strong voltage pulses can act as another resistance, which is beyond our stacked Josephson Junction model.

6.4 Modeling 1-D self-heating

We are not able to observe any relaxation oscillations when the device is latching. We believe that when the bias voltage is higher than the latching voltage point, the nanowire formulates a non-reversible hotspot that can not be thermally healed by the heat bath. Then the nanowire is believed to enter the third regime dominated by self-heating effect.

Carefully examining the I-V curve in Fig. 13 (a) and (b), we notice that there exist a series of zigzag current fluctuations with the increment of bias voltage. We anticipate that the self-heating hotspot expansion along one segment of the nanowire is quantized as resistance staircases. We suspect that those resistive steps are associated with granular nature of the ultra thin NbN thin films.

With the increment of dc voltage bias, a stable hotspot will develop at a certain section of the nanowire. The voltage width of the switched state depends also on the scanning direction and mode. Usually manually increasing the voltage will result in an accurate voltage point of the hotspot formation. Upon its formation, thermo-electrically Joule heating will apply. The first segment of the nanowires gradually exhibits normal state I-V properties as the dc bias voltage increases. The self-heating model by Skocpol *et al.* (Skocpol et al., 1974) is the best to account for this physical process. The current and voltage as the functions of the hotspot size χ_0 are

$$I_b(\chi_0) = I_r \sqrt{1 + \coth\left(\frac{\chi_0}{\eta_S}\right) \coth\left(\frac{\chi_0}{\eta_S} - \frac{L}{2\eta_n}\right)} \tag{7}$$

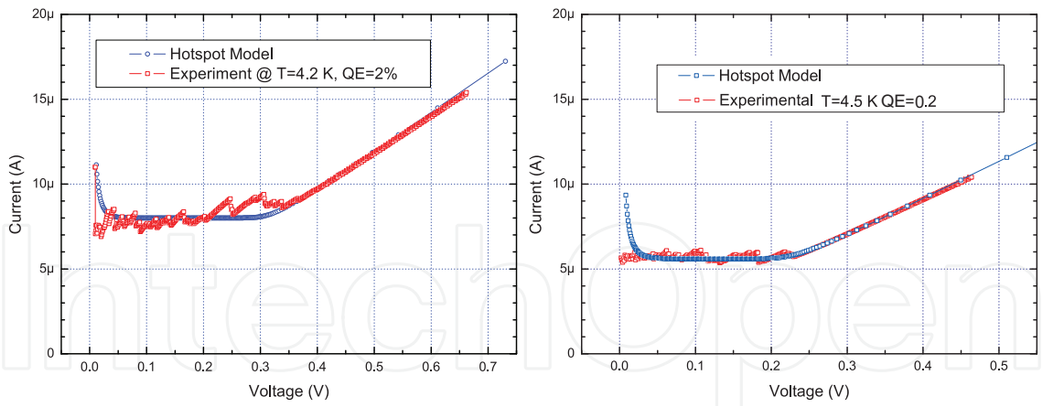

Fig. 13. Experimental and simulation results of the dc voltage and current characterization: (a) Hotspot formation under voltage bias, for DUT I; (b)Hotspot formation under voltage bias, for DUT II.

$$V_b(\chi_0) = I(\chi_0)\chi_0\rho_{20K}/Wd \tag{8}$$

in which we treat the thermal healing length η_S to be the same as η_n. The simulation results are displayed in Fig. 13 (a) and (b). The comparison to the experimental results shows a very good agreement between the theory and experiment. The parameters used in simulation are listed in Table 3.

In this model, one of the free parameters is ρ_{20K}, which can be extracted via the dc resistance measured during the sample cooling down. The notation of 20K can be understood as the maximum resistivity before the transition temperature T_c, which usually has the maximum value close to 20 K. The other free parameter, i.e. the return current I_r is determined from the I-V curve scan during the dc characterization measurement. It is the minimum current platform, almost constant current during the bias current. It may reveal the regularity along the segment of nanowire, because essentially this is based on one-dimensional ideal wire whose width is a constant of 120 nm, which can not be maintained to be true during the fabrication, i.e. the lithography. Our estimation based on this model shows that the thermal resistance is 0.048 Kcm^2/W at 4.2 K, which is a very good estimation based on self-heating model hot spots in (Skocpol et al., 1974). Note the range of χ_0 in Eqs. (7) and (8) is $a_0 < \chi_0 < l \sim 10\mu m$, in which a_0 is determined by Eq. 6 and assumed to be completely normal in this regime.

7. Summary

In this chapter, we first present the methods and results achieved from small signal RF/microwave measurement on the NbN nanowires. The equivalent circuit model is obtained via the two-step S-parameter measurement. We have justified the existence of R_s by checking the damped resonance frequency points under different dc voltage bias values (R_s increases when dc bias voltages increases). The theoretical calculation compares well to the experimental measurements when the R_s is large in the circuit model (see Fig. 1 (b)). The Ginsburg-Landau theory is employed to account for the L_k variation as the function of dc bias current ratio β. The analytical relation of L_k to β is obtained from G-L theorem. The weaklink effect is revealed to explain limitation of I_c from reaching the bulk I_c^{GL}. We also anticipate the device quality can be determined by the parametrical variation of the kinetic inductance, which we think it becomes a figure of merit for a given SNSPD in terms of its

quantum efficiency. Then we apply the small signal RF/microwave measurement method to investigate the thin film property. The measured results agrees with the expected value reported in the literature. This further confirms our method is a very effective tool to explore the change of Cooper pair density in the nanowires. Lastly, the I-V measurements showed four distinctive regime of a nanowire: i.e. superconducting, switched-relaxation, hotspot growth and hot wire regime, although the last regime is still under investigation, because not sufficient simulation has been carried on.

8. References

Z. Yan; M. K. Akhlaghi; JL. Orgiazzi; & A. H. Majedi (2009) Optoelectronic characterization of a fiber-coupled NbN superconducting nanowire single photon detector *Journal of Modern Optics*, vol. 56, pp. 380-4.

Z. Yan; A. H. Majedi & S. Safavi-Naeini, (2007) Physical Modeling of Hot-Electron Superconducting Single-Photon Detectors, *Applied Superconductivity, IEEE Transactions on*, vol. 17, pp. 3789-3794.

A. D. Semenov, P. Haas, B. Günther, H. -. Hübers, K. Il'in, M. Siegel, A. Kirste, J. Beyer, D. Drung, T. Schurig & A. Smirnov, (2007) An energy-resolving superconducting nanowire photon counter, *Superconductor Science and Technology*, vol. 20, pp. 919-924.

J. K. W. Yang, A. J. Kerman, E. A. Dauler, V. Anant, K. M. Rosfjord & K. K. Berggren, (2007) Modeling the electrical and thermal response of superconducting nanowire single-photon detectors, *IEEE Trans. Appl. Supercond.*, vol. 17, pp. 581-5.

M. Tinkham, J. U. Free, C. N. Lau & N. Markovic, (2003) Hysteretic I-V curves of superconducting nanowires, *Physical Review B*, vol. 68, pp. 134515-1.

S. Miki, M. Fujiwara, M. Sasaki, B. Baek, A. J. Miller, R. H. Hadfield, S. W. Nam & Z. Wang, (2008) Large sensitive-area NbN nanowire superconducting single-photon detectors fabricated on single-crystal MgO substrates, *Appl. Phys. Lett.*, vol. 92, pp. 061116.

R. H. Hadfield, P. A. Dalgarno, J. A. O'Connor, E. Ramsay, R. J. Warburton, E. J. Gansen, B. Baek, M. J. Stevens, R. P. Mirin & S. W. Nam, (2007) Submicrometer photoresponse mapping of nanowire superconducting single-photon detectors, *Appl. Phys. Lett.*, vol. 91, pp. 241108.

D. M. Pozar, (1998) *Microwave Engineering*. New York ; Chichester, England: John Wiley & Sons, ch-6.

K. S. Keskar, T. Yamashita, Y. Onodera, Y. Goto & T. Aso (1974) rf reactively sputtered superconducting NbN_x films, *Japn. J. Appl. Phys.*, vol. 45, pp. 3102-3105.

Y. M. Shy, L. E. Toth & R. Somasundaram (1973) Superconducting properties, electrical resistivities, and structure of NbN thin films *J. Appl. Phys.*, vol. 44, pp. 5539-5545.

J. Tyan and J. T. Lue (1994) Grain boundary scattering in the normal state resistivity of superconducting NbN thin films," *J. Appl. Phys.*, vol. 75, pp. 325-331.

R. T. Kampwirth and K. E. Gray, "NbN materials development for practical superconducting devices," *IEEE Trans. Magn.*, vol. 17, pp. 565-8.

K. E. Gray, R. T. Kampwirth, D. M. Capone II and R. Vaglio (1985) Microscopic investigation of NbN sputtered films *Physica B & C*, vol. 135B+C, pp. 164-7.

V. Ambegaokar and A. Baratoff, (1963) Tunneling between superconductors," *Phys. Rev. Lett.*, vol. 10, pp. 486-489.

V. Ambegaokar and A. Baratoff, (1963) Erratum: tunneling between superconductors," *Phys. Rev. Lett.*, vol. 11, pp. 104.

C. C. Chin, D. E. Oates, G. Dresselhaus & M. S. Dresselhaus (1992) Nonlinear electrodynamics of superconducting NbN and Nb thin films at microwave frequencies *Physical Review B (Condensed Matter)*, vol. 45, pp. 4788-98.

B. Abdo, E. Segev, O. Shtempluck & E. Buks (2006) Nonlinear dynamics in the resonance line shape of NbN superconducting resonators *Phys. Rev. B*, vol. 73, pp. 134513-11.

B. Bonin and H. Safa, (1991) Power dissipation at high fields in granular RF superconductivity *Supercond Sci Technol*, vol. 4, pp. 257-61.

T. P. Orlando, E. J. McNiff Jr., S. Foner & M. R. Beasley, (1979) Critical fields, Pauli paramagnetic limiting, and material parameters of Nb_3Sn and V_3Si *Physical Review B (Condensed Matter)*, vol. 19, pp. 4545-61.

M. W. Johnson, A. M. Herr & A. M. Kadin (1996) Bolometric and nonbolometric infrared photoresponses in ultrathin superconducting NbN films *J. Appl. Phys.*, vol. 79, pp. 7069-7074.

D. E. Oates, A. C. Anderson, C. C. Chin, J. S. Derov, G. Dresselhaus & M. S. Dresselhaus, (1991) Surface-impedance measurements of superconducting NbN films *Phys. Rev. B*, vol. 43, pp. 7655-63.

M. Lindgren, M. Currie, C. A. Williams, T. Y. Hsiang, P. M. Fauchet, R. Sobolewski, S. H. Moffat, R. A. Hughes, J. S. Preston & F. A. Hegmann, (1996) Ultrafast photoresponse in microbridges and pulse propagation in transmission lines made from high-Tc superconducting Y-Ba-Cu-O thin films *IEEE Journal of Selected Topics in Quantum Electronics*, vol. 2, pp. 668-78.

R. H. Hadfield, A. J. Miller, S. W. Nam, R. L. Kautz and R. E. Schwall (2005) Low-frequency phase locking in high-inductance superconducting nanowires *Appl. Phys. Lett.*, vol. 87, pp. 203505-1.

W. J. Skocpol, M. R. Beasley & M. Tinkham, (1974) Self-heating hotspots in superconducting thin-film microbridges *J. Appl. Phys.*, vol. 45, pp. 4054-66.

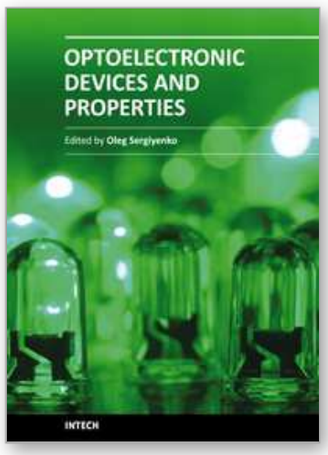

Optoelectronic Devices and Properties

Edited by Prof. Oleg Sergiyenko

ISBN 978-953-307-204-3
Hard cover, 660 pages
Publisher InTech
Published online 19, April, 2011
Published in print edition April, 2011

Optoelectronic devices impact many areas of society, from simple household appliances and multimedia systems to communications, computing, spatial scanning, optical monitoring, 3D measurements and medical instruments. This is the most complete book about optoelectromechanic systems and semiconductor optoelectronic devices; it provides an accessible, well-organized overview of optoelectronic devices and properties that emphasizes basic principles.

INTECH
open science | open minds

InTech Europe
University Campus STeP Ri
Slavka Krautzeka 83/A
51000 Rijeka, Croatia
Phone: +385 (51) 770 447
Fax: +385 (51) 686 166
www.intechopen.com

InTech China
Unit 405, Office Block, Hotel Equatorial Shanghai
No.65, Yan An Road (West), Shanghai, 200040, China
中国上海市延安西路65号上海国际贵都大饭店办公楼405单元
Phone: +86-21-62489820
Fax: +86-21-62489821

IntechOpen